Chapter 2
An in-situ Grain-resolved Study of FCC Nickel Plasticity over Gross Granular Fields using Digital Image Correlation with High Resolution Optical Microscopy

Olcay Türkoğlu and C. Can Aydıner

Abstract A recent implementation (Türkoğlu, O., Aydıner, C., *Exp Mech* **64**: 655–674, 2024) of optical-microscopy digital image correlation [OM-DIC] employs high numerical aperture [NA] objectives despite their limited depth of fields, by fending off continual defocusing via automated working distance maintenance. Combining this OM-DIC variant that maximizes optical resolution with robust area scanning, field coverage is expanded to the millimeter scale, capturing deformation of thousands of grains in the region of interest. In this study, grain maps are also produced to enable a grain-resolved study of deformation fields; the orientations of each grain are further assigned by electron backscatter diffraction conducted prior to the OM-DIC experiment. An FCC pure Nickel polycrystal specimen is elected with an average of 25 μm grain size. 40x microscopy with the high-NA (=0.42) objective yields on the order of 10^3 DIC points per grain. During the uniaxial load application up to 5% tensile strain, in-situ OM-DIC data is collected at three steps (1.65%, 3.34% and 5%, respectively) to investigate the evolution of intra-grain and inter-grain plastic deformation, as well as interactions between neighboring grains. Accurate grain mapping enables precise segmentation of the grain boundaries, facilitating the extraction of deformation and rotation signals for each individual grain, distinguishing grain cores and grain mantles (the band around the boundary of a grain with each of its neighbors). Given this framework, the objectives of this study are twofold: (i) to derive statistical correlations between mantle and core deformation/rotation of individual grains as a function of crystallographic orientation, and (ii) to derive statistical correlations between sibling mantles (that share the same grain boundary but located in different grains).

Keywords optical microscopy · DIC · polycrystal · high resolution · grain-resolved · grain boundary deformation

Introduction

Digital image correlation has become a prominent strain field measurement technique for both industrial and academic uses. Despite the limited resolution compared to electron microscopy, academic applications [1–4] of DIC combined with optical microscopy provide a measurement capability across different length-scales. These applications are expanding the knowledge of deformation heterogeneity of metallic materials while providing measurement data for calibration of high-fidelity plasticity models [5, 6]. Current applications of OM-DIC have been advancing accuracy and resolution limits by implementing a novel methodology that uses high numerical aperture optics combined with robust area scanning for immense statistics [1–3] and, most recently, extracts strain fields over every individual grain by generating grain masks [7, 8]

Classifying deformation fields into type-I (macroscopic/aggregate average), type-II (intergranular, $\overline{\varepsilon}$), and type-III (intragranular, ε), an OM-DIC setup that can capture type-III strains and calculate the rest by averaging requires high magnification and high numerical aperture (NA) optics. However, these optical settings make the implementation prone to defocusing due to the associated limited depth of field (on the order of a few μm) and are prone to limited field coverage that results from

Olcay Türkoğlu (✉)
Department of Mechanical Engineering Işık University, Sile, Istanbul, 34980, Türkiye
*Corresponding author. e-mail: olcay.turkoglu@isikun.edu.tr

C. Can Aydıner
Department of Mechanical Engineering Boğaziçi University, Bebek, Istanbul, 34342, Türkiye
e-mail: can.aydiner@bogazici.edu.tr

Chi-Hung Hwang et al. (eds.), *Advancement of Optical Methods & Digital Image Correlation in Experimental Mechanics, Vol. 2*, Conference Proceedings
of the Society for Experimental Mechanics Series, https://doi.org/10.13052/97887-438-0828-2_2

increased magnification [9]. To address these limitations, this in-house-built OM-DIC setup [1, 2, 7, 8] incorporates an automated working distance maintenance algorithm for precise focusing and a robust area scanning implementation to extend the coverage to millimeter scales. As a result, an average-sized grain in the current study contains on the order of 10^3 subsets (grain-resolved, type-III signals). With full field coverage extended to millimeters, thousands of such grains are sampled, making type-II strains (strains averaged over the domain of each grain) statistically meaningful as well. Furthermore, the high resolution enables averaging over any chosen material subset, e.g, the individual boundary among neighboring grains. While the intragrain data resolution (grain-resolved resolutions) are generally produced with scanning electron microscopy [SEM]-DIC [10, 11] with at times two order higher resolution, the current OM-DIC variant strives to offer meaningful data for polycrystal physics with its higher practicality (leading to abundant in situ data at multiple load points) and high granular statistics.

Here, an FCC pure Nickel polycrystal sample is evaluated due to its simple deformation mechanism and is less likely to exhibit twinning because of relatively high stacking fault energy (90mJ/m^2 [12]). Although deformation of the highest-symmetry FCC metals is considered homogenous in the macro-scale, deformation on the microscale is complex and heterogeneous. Recent studies [5, 6] show that even the elastic deformation of pure Nickel polycrystals is heterogeneous at the intragranular scale. It is commonly postulated [13, 14] that one of the sources of this deformation heterogeneity is accumulation of deformation at the triple-point regions and boundary regions. However, these strain accumulations and difference between grain-boundary and grain-core region deformation are reported for only a few grains in the polycrystalline aggregates [13, 14]. On the other hand, these strain accumulations are observed in different sizes of boundary segments within grains (in order of nanometers to few micrometers). The best of the authors' knowledge, a methodology that statistically investigates core and boundary deformation over relatively large material field is missing. This study aims to lay out certain features of such a methodology with a particular focus on deformation differences over grain-boundary regions (mantle) and core regions in a statistical manner.

Experimental

Commercially pure (99.5%) face-centered-cubic [FCC] Nickel rod (extruded) with 6.25 mm diameter is procured from Alfa-Aesar (Thermo Fisher). The rod was subjected to annealing heat treatment (4 hours at 800^o C) and is fully recrystallized, and grain-growth is established (final average grain size: 25 μm). The dog-bone specimen (8 mm gage length and 3x3 mm^2 gage cross section) was precisely machined using wire electric discharge machining [WEDM]. The longitudinal (loading) direction of the tensile specimen was aligned with the extrusion direction of the rod. During the metallography, gradual grinding and extensive polishing with colloidal silica (5nm-particle-size) was applied carefully with automatic grinding machine (QATM Saphire 530). Subsequently, the specimen was minimally etched with diluted Marble's reagent to reveal boundaries without topographic distortions on the grains' surfaces. Prior to the tensile test, specimen was subjected to electron backscattering diffraction [EBSD] and crystallographic orientations of individual grains in the region of interest [ROI] were gathered via AMATEK EDAX detector in a FEI Quanta 400 FEG SEM.

The custom DIC setup depicted in Figure 1 (a) comprises several key components. First, there are the stationary optical lines, which include a macroscopic line—featuring a FLIR Grasshopper 3 camera with a 2.3 MP Sony IMX174 monochrome sensor and an Edmund Optics 0.5x telecentric lens—and a microscopic line, which uses another FLIR Grasshopper 3 camera equipped with a 5 MP Sony IMX250 monochrome sensor, a Navitar Ultrazoom 6000 tube lens, and a high-NA (=0.42) Mitutoyo M Plan APO 20x objective with a 0.1 μm/pixel field length. Second, the setup includes a small form factor tension-compression load frame (10 kN, Kammrath & Weiss). Third, an X-Y-Z positioning array (Newport M-ILS series for X-Y and GTS30V for the vertical Z positioner) is employed. The entire system is mounted on a Newport RS4000 vibration isolation table, and in-house instrument software automates the coordination of both the cameras and the stage motions.

Continuous strain monitoring is conducted under the macroscopic line using live macro-DIC analysis during the tensile test. At selected load steps shown in Figure 1 (b), the sample is transferred beneath the micro-DIC line, where micro-DIC area scans (X-Y) capture the images of the surface over a predefined grid of overlapping frames. These overlaps facilitate the seamless merging of both image and data fields (e.g., strain). In this experiment, the frame matrix consists of 13×7 images covering an overall ROI of approximately 2×0.8 mm^2. (Images of this domain and further details of sample and setup are provided elsewhere [8]; a study that uses different data from the same experiment to explore elastics strain upon unloads and the possibility to evaluate stresses.)

DIC analysis is performed using a Gauss-Newton inverse composition algorithm with 61×61 pixel subsets (6×6 μm^2) and 10 pixels (1 μm) grid spacing. The gradient of the displacement then calculated by using 3×3 Savitzky-Golay differentiation kernel to determine local strains [15].

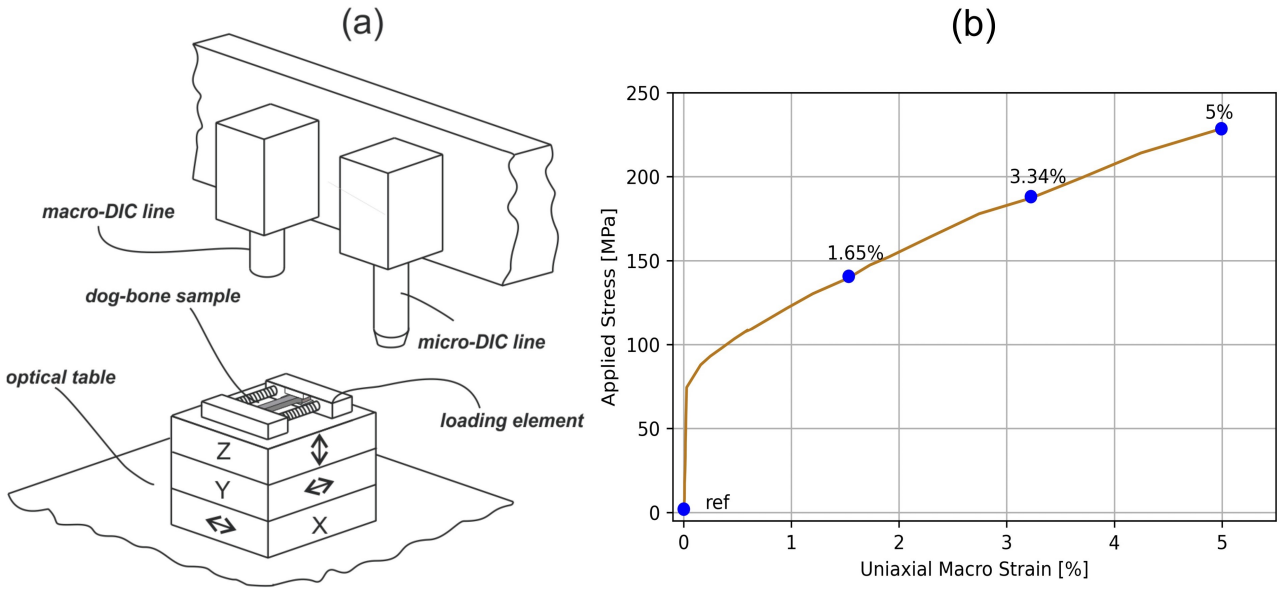

Fig. 1 (a) Experimental setup, (b) Macro tensile curve

Before the in-situ micro-DIC experiment and speckle pattern application (but after metallography to reveal grain boundaries), a complete area-scan is conducted to image the full ROI. Avoiding the concealing effect of the speckles on grain boundaries, an accurate grain mask (boundary map) that enables the extraction of grain-resolved information is manually generated over this image, using precise Bezier curves. The grain mask is then compared/verified with the grains identified in the EBSD analysis, and the crystallographic orientations are registered for each identified grain. Approximately 3000 grains are identified/indexed with their exact morphology (grain mask) and crystallographic orientation. Subsequently, the speckle pattern is applied using a unique method prior to the reference DIC scan. Finally, the grain mask undergoes a precise affine transformation to correct for small tilts and distortions introduced during the demounting and remounting of the tensile specimen, before and after the speckle pattern application (see [8] for details of the grain mask extraction procedure). As a result, the image fields of the reference load point and the utilized grain mask are exactly aligned. The micro-DIC experiment is conducted in-situ, with micro-DIC conducted at multiple loading points as the tensile load is advanced in position control. Figure 1 (b) shows the three field-average strain levels up to 5% where results are presented in this paper.

The defining trait of postprocessing in this type of study is to explore strains per grain, and over other polycrystal morphological features, e.g., material bands about grain boundaries. For this, after the experiment and DIC analyses are conducted, strain signal of each grain is processed with morphological operations. First, strains over grain boundaries are discounted, using a binary erosion algorithm over the grain mask. [Although a DIC speckle pattern should be random and isotropic, continuous lines of the grain boundaries in OM images compromise these aspects. As a result, a possible source of DIC error is eliminated. The data over grain boundaries do not belong to any individual grain anyways.] Secondly, after this initial peeling of the outer layer of the grain (discounting red zones in Figure 2), more layers (n, up to 5) are removed, as schematically shown in the light grey lines for n=2 in Figure 2. The region of each grain around its core that is bounded by the gray (n=2, two-layer-stripped) boundaries will be referred to as the grain core in the rest of the text. However, the boundary obviously loops through multiple neighboring grains (a total of 7 neighbors for the central grain in Figure 2) and we propose to investigate each boundary segment independently. To this end, another morphological algorithm slices the overall boundary region with lines that connect the centroids [CM] of each grain and triple points. An imaginary triangular slice of the relevant grain is extracted via a CM and triple points (refer to dashed grey lines in Figure 2); then, an inward binary dilation algorithm is applied to the boundary segment of this slice multiple times (n, up to 5). As a result, bands of material inside a grain that is closest to each neighboring grain are distinguished. As such one can extract the strains of the central grain in the vicinity of its boundary with neighbor 1. This region is called the mantle 0-1 on Figure 2; indicating the band region inside grain 0 but neighboring grain 1. The opposite mantle region inside grain 1 is analogously called mantle 1-0.

The CM-to-triple-point bisection prevents the repetitive use of subsets near the boundary region, ensuring that the average strain for each mantle (0-1, 0-2, etc.) is computed from non-overlapping data. After generating masks for both the core and mantle regions of the grains, the DIC strain signals inside each grain (type-III) are locally averaged over both regions. The result of this operation is shown in Figure 2 for axial strains with a colormap.

Results and Discussion

Local results from the exemplified neighborhood

Following the average strain extraction method described in the previous section, a sample neighborhood is selected within the overall ROI [8], as indicated in Figure 2. At the center of this neighborhood, an average-sized grain (grain 0) is highlighted, with its mantle and core regions depicted in colors corresponding to their respective average axial strain values at 5% macroscopic strain. While the average axial core strains of some neighboring grains (n3, n4) are comparable to the applied macroscopic strain, others (n1, n5, n6) exhibit larger strain values. Considering that the neighborhood is relatively small (approximately $40 \times 40\mu\,\mathrm{m}^2$), these variations in average axial strain across local regions (which can be deemed type-II strains) are significant (numerical values are provided in Table 1).

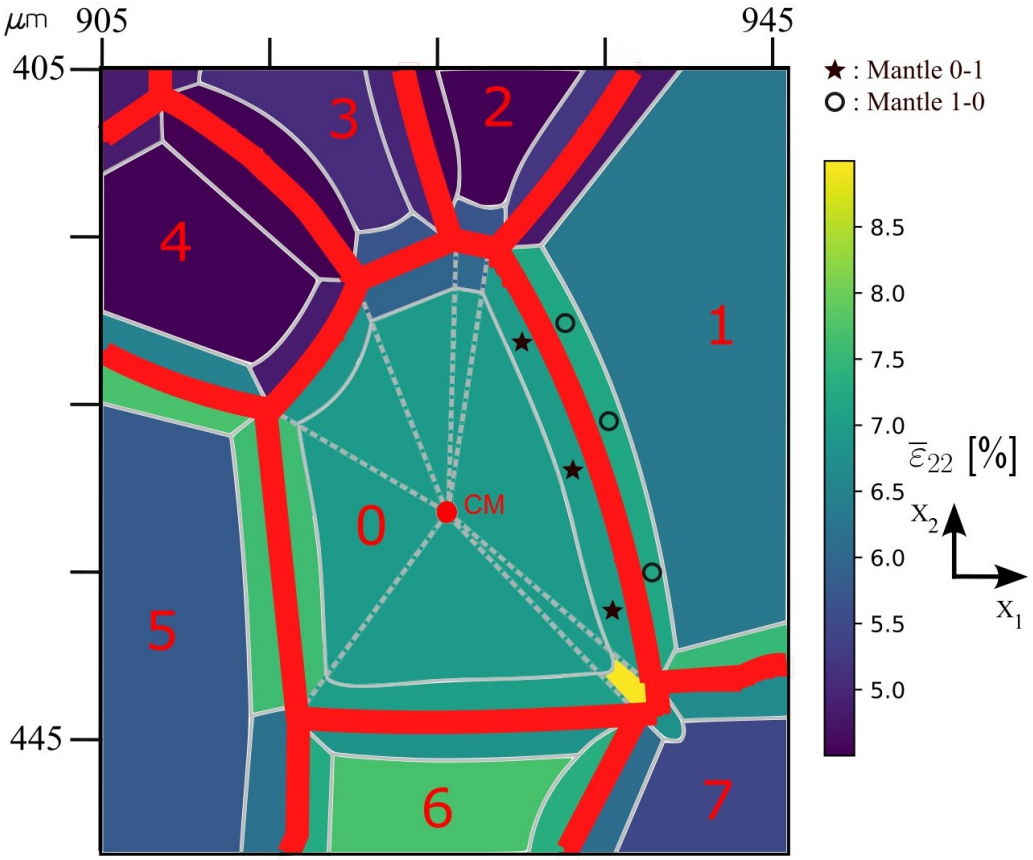

Fig. 2 Mantle-averaged and core-averaged strains of the selected grain and neighboring grain cores and mantles (n=2)

Table 1 presents the average strain values for both the axial and transverse directions for the sample neighborhood. The column headers indicate the neighboring grain numbers, while the row headers list E_{hkl} (directional stiffness along tensile direction), in-grain mantle strains (e.g. Mantle 0-1, Mantle 0-2, etc.), in-neighbor mantle strains (e.g. Mantle 1-0, Mantle 2-0, etc.) and core strains of neighboring grains. The mantles 0-2 and 0-7 are, however, too small to draw conclusions from and the corresponding rows in Table 1 are shaded gray. In case of $\bar{\varepsilon}_{11}$, the average mantle strains within the center grain vary from –0.7% to –2.8%, indicating a higher degree of dispersion in transverse strains compared to the axial strain, $\bar{\varepsilon}_{22}$. Interestingly, even among neighboring mantles(e.g., Mantle 0-1 and Mantle 1-0), the average transverse strains can differ significantly (–1.3% vs. –4.7%), which is consistent with the large differences in transverse strains among the core strains in the neighborhood (core 0: –1.7%; core 1: –4.0%). Axial strain, in contrast, are quite more regulated. Similar observations have been made for elastic strains (upon unload) [8].

Additionally, the directional stiffness—calculated based on crystallographic orientation ascertained by prior EBSD—of neighboring grains may be an important effective factor behind the observed deformation heterogeneity. For example, the center grain exhibits relatively high directional stiffness, while grain n1 has the lowest and n6 has a stiffness similar to that

of the center grain. However, the axial and transverse strain averages in these neighborhoods (0-1 and 0-6) do not show a direct correlation between directional stiffness and the average strains accumulated over the boundaries or core regions at 5%, i.e., significant plastic strain. The data is analyzed with a statistically sufficient number of grains for this and similar correlations currently and the findings will be shared elsewhere in the future. Some aspects of the strain variation across the full-field (entire ROI) that focuses on core-mantle variations is presented in the next section.

Table 1 Mantle-averaged and core-averaged strains of the selected grain and neighboring grain cores and mantles

	n1	n2	n3	n4	n5	n6	n7
E_{hkl} [GPa] (Center Grain: 302GPa)	148	297	159	227	164	302	265
Mantle Strain ($\bar{\varepsilon}_{22}$) (in-grain) [%]	6.9	6.0	6.0	6.9	7.6	7.0	9.8
Mantle Strain ($\bar{\varepsilon}_{22}$) (in-neighbor) [%]	7.2	5.8	5.7	5.0	7.6	6.8	6.8
Core Strain ($\bar{\varepsilon}_{22}$) [%] (Center Grain: 7%)	6.4	4.5	5.0	4.3	5.8	7.6	5.6
Mantle Strain ($\bar{\varepsilon}_{11}$) (in-grain) [%]	-1.3	-0.1	-0.7	-1	-2.8	-2	-5
Mantle Strain ($\bar{\varepsilon}_{11}$) (in-neighbor) [%]	-4.7	0.3	-0.7	-1.2	0	-2.7	-4.4
Core Strain ($\bar{\varepsilon}_{11}$) [%] (Center Grain: -1.7%)	-4.0	-0.8	-1.5	-1.6	-1.2	-3	-2.4

Statistical (full-field) results

Statistical results for all mantles/cores (as defined in the sample domain of Figure 1) are drawn from the entire ROI as long as the grains meet the following criteria for strain/orientation data health: (i) grain size should be larger than 12μ m, ensuring that at least approximately 100 subsets are available in the grain-resolved domain, (ii) grains are not located in the stitching region among individual frames of the area-scan [8], and (iii) grains have a high EBSD confidence index ($CI > 0.65$). After this filtering, a total of 1290 grains are obtained, comprising 7823 mantles overall.

From a statistical point of view, first, average strain distributions of mantle and core regions are investigated at each load point. However, histograms are not used to present these distributions because the total number of core regions and mantle regions are not equal (which yields much more different frequencies on the y-axis of regular histograms, comparing histograms becomes difficult). Instead of histograms, Weibull probability density functions are fitted to all strain distributions and these are presented. Unlike the more typical Gaussian distributions, Weibull distributions allow asymmetrical distributions and provide statistically better fits for surface strain components, $\bar{\varepsilon}_{11}$, $\bar{\varepsilon}_{22}$ and $\bar{\varepsilon}_{12}$. Therefore, the following figures in this are represented as Weibull distribution with probability densities. The minimum r^2 value in the fits is calculated as 0.97 that justifies the use of Weibull fits to the data in this presentation .

In Figure 3 (a-c), surface strain components $\bar{\varepsilon}_{11}$, $\bar{\varepsilon}_{22}$ and $\bar{\varepsilon}_{12}$ are presented, respectively. Each part, contains results for all load points (macroscopic strains 1.65, 3.34 and 5%) to present the evolution of the distributions. The results are distinguished over the core (solid lines) and mantle (dashed lines) regions. As a result, the first apparent conclusion that can be drawn from these distributions is that the mantle distributions exhibit a higher strain range. Moreover, as macroscopic strain increases, the strain range in the mantles tends to increase, along with increase in strain heterogeneity between grains. The reduction in probability density combined with the increase in strain range after the load increment clearly demonstrates this behavior. While most reports in the literature indicate that mantles (more precisely, grain boundary segments) accumulate high strains [3, 9, 10], the distributions in Figure 3 (a–c) reveal that some mantle regions exhibit smaller strains than the core, even though most mantles show strain levels similar to those of the cores. Note $\bar{\varepsilon}_{12}$ median values are approximately equal to zero in this uniaxial loading, which can be considered as a sanity check. Similarly, the median/mean ratios of normal strains ($-\bar{\varepsilon}_{11}/\bar{\varepsilon}_{22}$, Poisson's ratio) yields the expected 0.5. Over a full statistical average (also equivalent to averaging of the shown distributions), strains in the mantle regions are similar to those in the core regions, i.e., there is no apparent higher strain in the mantles.

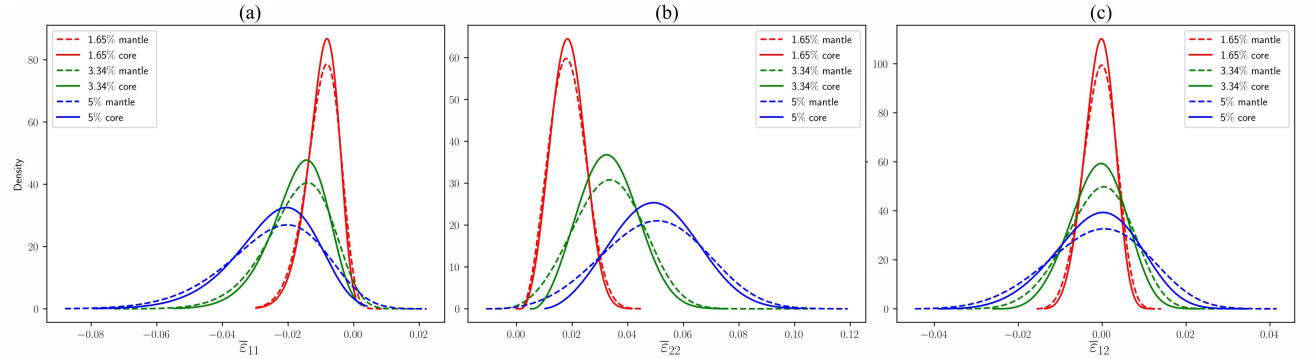

Fig. 3 Strain distribution evolution of core and mantle strains (a) $\overline{\varepsilon}_{11}$, (b) $\overline{\varepsilon}_{22}$ and (c) $\overline{\varepsilon}_{12}$

A more compound metric is considered next in Figure 4, delineating the local difference between mantle and core strains. For this, the average strains of each mantle are normalized by the average strain at the core of the particular grain. Figure 4 (a-c) shows these normalized strain distributions. As a general result, median values of these strain ratios are approximately equal to one, supporting the notion that the highest fraction of mantles and cores have similar strains in this polycrystalline aggregate. Core-normalized $\overline{\varepsilon}_{22}$ ($\overline{\varepsilon}_{22\ mantle}/\ \overline{\varepsilon}_{22\ core}$) distributions (Figure 4 (b)) seem more regularized than other strain components which are expected due to their alignment with the tensile direction. While macroscopic strain increases, core-normalized $\overline{\varepsilon}_{22}$ distributions show a tendency to spread. In particular, when 1.65% and 3.34% macroscopic strains are compared, range of core-normalized $\overline{\varepsilon}_{22}$ increases significantly. However, when the macroscopic strain increased from 3.34% to 5%, the increase in the range of core-normalized $\overline{\varepsilon}_{22}$ is limited. A similar behavior is also observed for core-normalized $\overline{\varepsilon}_{11}$ and $\overline{\varepsilon}_{12}$ (Figure 4 (a), (c)), however the range of strain ratios differs significantly as well as probability densities. Since the nominal value of $\overline{\varepsilon}_{12}$=0, large values tend to occur with both positive and negative senses in Figure 4 (c), which should not be assigned a physical significance. Core-normalized $\overline{\varepsilon}_{11}$ shows a larger spread than core-normalized $\overline{\varepsilon}_{22}$, in line with the previous observations.

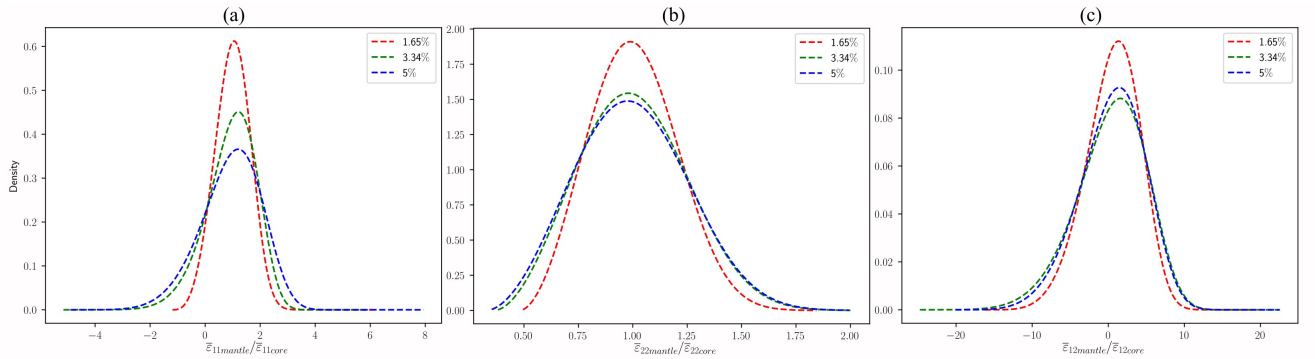

Fig. 4 Strain ratio of mantle and core strains at 5% macroscopic strain, (a) $\overline{\varepsilon}_{11\ mantle}/\ \overline{\varepsilon}_{11\ core}$, (b) $\overline{\varepsilon}_{22\ mantle}/\ \overline{\varepsilon}_{22\ core}$ and (c)

The mantle thickness in the above evaluations have been taken as two data layers of grains (each layer approximately 1 μm thick). Figure 5 (a-c) studies the dependence of the shown results on the assumed mantle band thickness. Thicknesses up to 6 data layers (6 μm) are considered and the average strain response of the mantles are shown. Although, 5% macroscopic load point which shows the most dispersive average strain behavior for mantles is selected, the variance of the Weibull distributions of different mantle thickness still shows a very similar behavior and no significant difference is observed in both ranges and probability densities. (Note that one-layer-thick mantles are not included in computations to increase numbers of the subsets in the averaging zone.) Consequently, the distributions shown are robust against mantle thickness variations.

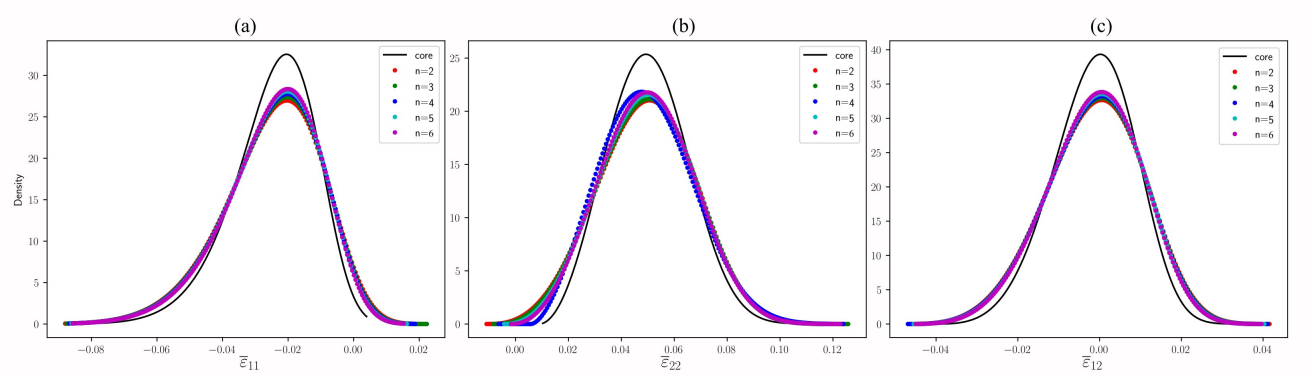

Fig. 5 Strain distribution response of varying mantle band widths (n=2,..,6 roughly corresponds to n=2,..,6 μm) at 5% macroscopic strain (a) $\overline{\varepsilon}_{11}$, (b) $\overline{\varepsilon}_{22}$ and (c) $\overline{\varepsilon}_{12}$

Conclusion

To conclude, this OM-DIC variant, which employs high numerical aperture and high magnification optics, provides a field resolution comparable to that achieved in coarse SEM-DIC applications, thereby enabling grain-resolved deformation research. Furthermore, robust area scanning expands the coverage to millimeter scales while capturing deformation signals for thousands of grains. This preliminary study offers a prospective framework that demonstrates differences in strains between the core and mantle regions of individual grains in a polycrystalline aggregate. As shown in the exemplified results, even though the analyzed neighborhood is relatively small (approximately $40 \times 40\mu\ \mathrm{m}^2$), significant deformation heterogeneity is observed both within individual grains and across the local neighborhood. The full-field results contain deformation statistics that compare core and mantle regions. In future work, these statistics will be further investigated by considering factors such as directional stiffness, Schmidt factors, grain-resolved rotation, and variations in core and mantle sizes, thereby advancing our understanding of deformation heterogeneity and facilitating experimental comparisons with high-fidelity plasticity models.

Acknowledgments O.T. acknowledges the financial support of the Scientific and Technological Research Council of Turkey (TÜBİTAK) through the 2224-A Grant Program and Işık University, which enabled travel and participation in the 2025 SEM Annual Conference.

References

1. Shafaghi N, Kapan E, Aydıner CC, Cyclic Strain Heterogeneity and Damage Formation in Rolled Magnesium Via In Situ Microscopic Image Correlation, Exp Mech, 60:735–751, 2020, https://doi.org/10.1007/s11340-020-00612-6
2. Özdür NA, Üçel IB, Yang J, Aydıner CC, Residual Intensity as a Morphological Identifier of Twinning Fields in Microscopic Image Correlation, Exp Mech, 2020 https://doi.org/10.1007/s11340-020-00672-8
3. Aydıner CC, Telemez MA Multiscale deformation heterogeneity in twinning magnesium investigated with in situ image correlation, Int J Plast 56:203–218, 2014 https://doi.org/10.1016/j.ijplas.2013.12.001
4. Carroll, J., W. Abuzaid, J. Lambros and H. Sehitoglu, "An Experimental Methodology to Relate Local Strain to Microstructural Texture", Review of Scientific Instruments, Vol. 81, No. 8, p. 83703, 2010, https://doi.org/10.1063/1.3474902
5. P. Eisenlohr, M. Diehl, R.A. Lebensohn, F. Roters, A spectral method solution to crystal elasto-viscoplasticity at finite strains, Int J Plast, 46:37-53, 2013. https://doi.org/10.1016/j.ijplas.2012.09.012
6. Jiahao Cheng, Jinlei Shen, Raj K. Mishra, Somnath Ghosh, Discrete twin evolution in Mg alloys using a novel crystal plasticity finite element model, Acta Mater, 149:142-153, 2018, https://doi.org/10.1016/j.actamat.2018.02.032
7. Türkoğlu, O. and C. C. Aydıner, "Enabling Digital Image Correlation with High Resolution Microscopic Optics via Working Distance Automation: Advancing Resolution and Accuracy Limits", SEM2022: Advancements in Optical Methods, Digital Image Correlation & Micro-and Nanomechanics, Vol. 4, pp. 49–56, Springer International Publishing, Cham, 2023, https://doi.org/10.1007/978-3-031-17471-1_9
8. Türkoğlu, O., Aydıner, C. An Exploration of Grain-Averaged Stress Measurement Using Partial Unloads with In situ Microscopic Image Correlation, Exp Mech 64:655–674, 2024. https://doi.org/10.1007/s11340-024-01050-4
9. Padilla HA, Lambros J, Beaudoin AJ, Robertson IM, Relating inhomogeneous deformation to local texture in zirconium through grain-scale digital image correlation strain mapping experiments. Int J Solids Struct, 49:18–31, 2012, https://doi.org/10.1016/j.ijsolstr.2011.09.001
10. J.C. Stinville, N. Vanderesse, F. Bridier, P. Bocher, T.M. Pollock, High resolution mapping of strain localization near twin boundaries in a nickel-based superalloy, Acta Mater, 98:29-42, 2015 https://doi.org/10.1016/j.actamat.2015.07.016.

11. Kammers, A.D., Daly, S. Self-Assembled Nanoparticle Surface Patterning for Improved Digital Image Correlation in a Scanning Electron Microscope. Exp Mech, 53:1333–1341, 2013. https://doi.org/10.1007/s11340-013-9734-5
12. Hertzberg, R. W., Deformation and Fracture Mechanics of Engineering Materials,4th edn., J. Wiley & Sons, New York, 1996.
13. H.-H. Fu, D.J. Benson, M.A. Meyers, Analytical and computational description of effect of grain size on yield stress of metals, Acta Mater, 49-13: 2567-2582 2001, https://doi.org/10.1016/S1359-6454(01)00062-3
14. Wael Z. Abuzaid, Michael D. Sangid, Jay D. Carroll, Huseyin Sehitoglu, John Lambros, Slip transfer and plastic strain accumulation across grain boundaries in Hastelloy X, J. Mech. Phys. Solids. 60-6:1201-1220, 2012, https://doi.org/10.1016/j.jmps.2012.02.001
15. Pan, B., K. Li and W. Tong, Fast, Robust and Accurate Digital Image Correlation Calculation Without Redundant Computations, Exp Mech, 53:1277–1289, 2013, https://doi.org/10.1007/s11340-013-9717-6